

Automated Segmentation of Lesions in Ultrasound Using Semi-pixel-wise Cycle Generative Adversarial Nets

Jie Xing, Zheren Li, Biyuan Wang, Bingbin Yu, Farhad G. Zanjani, Aiwun Zheng, Remco Duits, Tao Tan

Abstract—Breast cancer is the most common invasive cancer with the highest cancer occurrence in females. Handheld ultrasound is one of the most efficient ways to identify and diagnose the breast cancer. The area and the shape information of a lesion is very helpful for clinicians to make diagnostic decisions. In this study we propose a new deep-learning scheme, semi-pixel-wise cycle generative adversarial net (SPCGAN) for segmenting the lesion in 2D ultrasound. The method takes the advantage of a fully convolutional neural network (FCN) and a generative adversarial net to segment a lesion by using prior knowledge. We compared the proposed method to a fully connected neural network and the level set segmentation method on a test dataset consisting of 32 malignant lesions and 109 benign lesions. Our proposed method achieved a Dice similarity coefficient (DSC) of 0.92 while FCN and the level set achieved 0.90 and 0.79 respectively. Particularly, for malignant lesions, our method increases the DSC (0.90) of the fully connected neural network to 0.93 significantly ($p < 0.001$). The results show that our SPCGAN can obtain robust segmentation results. The framework of SPCGAN is particularly effective when sufficient training samples are not available compared to FCN. Our proposed method may be used to relieve the radiologists' burden for annotation.

Index Terms—Lesion Segmentation, Deep Learning, Generative Adversarial Networks, Breast Cancer, Ultrasound Image Analysis

I. INTRODUCTION

Breast cancer is one of the leading causes of death for women in the UK. According to the statistics published by Cancer Research UK, there are about 155 women in 100,000 suffering from breast cancer in the UK and incidence rate is around 10% for females in other European countries while this number is over 12.5% for breast cancer with the American females [1]. Since the causes of breast cancer still remain unknown, early diagnosis of breast cancer plays a significant role in reducing the death rate and maintaining the quality of the life after treatments [2].

Ultrasound imaging technology has developed rapidly in recent years. Compared to mammography, there is no radiation damage to women from ultrasound imaging. It is easy to obtain any cross-sectional images of breast tissue by manipulating the handheld ultrasound while normally only two projections are obtained from mammography. It provides an easy way to assess if a lesion is solid or fluid-filled [3]. Ultrasound detects early-stage cancers in women

with mammography-negative dense breasts, with higher contribution in women younger than 50 years [4]. Moreover, breast ultrasound is simple, effective and low cost. Because of all these advantages, it can be applied in a large scale for imaging, for example, in China [5].

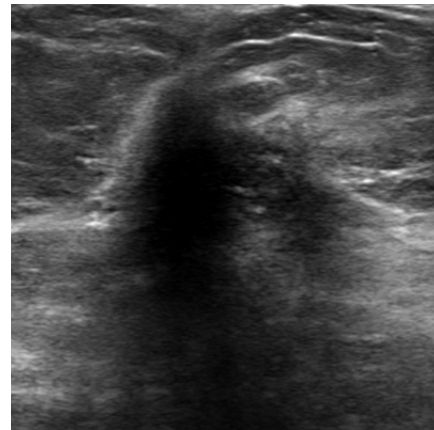


Fig. 1. A malignant lesion in breast ultrasound

In the clinical workflow of breast ultrasound imaging, radiologists often report the sizes of breast lesions, describe the lesions according to BI-RADS lexicon [6] and estimate the final BI-RADS score. An accurate delineation of breast lesion can help radiologists to describe margin, shape and posterior features. However, manual segmentation of breast lesions is time-consuming and tedious. The segmentation also varies from one reader to another. Therefore, the automated segmentation can play a key role in facilitating the reporting of the diagnosis. In terms of detection and diagnosis, computers can also assist radiologists to make decisions that improve the effectiveness of ultrasound reading. For example, computer techniques [7]–[12] have been proposed to delineate the contour of lesions or directly detect or diagnose breast lesions. Most of these computer-aided diagnoses or detections include a module of segmentation. Therefore, it is important to develop a robust and accurate segmentation method.

Breast lesion segmentation is very challenging, especially when there is the presence of noise, the ill-defined edges, irregular shapes, and different posterior behaviors of lesions. As Fig. 1 shows, there is strong shadowing in the posterior and upper region, the lesion boundary is fuzzy and not clear. Therefore, there is a risk that segmentation algorithms fail, causing oversegmentation.

There are two types of segmentation methods: contour-based and region-based methods. The contour-based segmentation relies on finding the optimal contour to enclose the whole breast lesion. Region-based methods aim to assign a label to every image pixel. Jing et al. [13] proposed an iterative segmentation scheme to refine the initial contour and perform self-examination and correction on the segmentation result. Their best intersection of the computer and the reference segmented area was 0.84. Tan et al. [14] proposed a novel depth-dependent dynamic programming technique and obtained a Dice similarity coefficient (DSC) of 0.73. This accuracy was then

Jie Xing, Zheren Li have equal contribution
 J. Xing and Ai-Wen Zheng are with Zhejiang cancer hospital, China
 Z. Li is with Department of Bioengineering, Imperial College London, London SW7 2AZ, UK
 T. Tan and R. Duits are with Department of Mathematics and Computer Science, Eindhoven University of Technology, Eindhoven 5600 MB, The Netherlands
 Farhad G. Zanjani is with Department of Electrical Engineering, Eindhoven University of Technology, Eindhoven 5600 MB, The Netherlands
 B. Wang is with Department of Computing, Tokyo Institute of Technology, Tokyo, Japan
 B. Yu is with Robotic Innovation Center, German Research Center of Artificial Intelligence, Bremen, Germany
 T. Tan (t.tan1@tue.nl) is the corresponding author

improved by Kozegar et al. with a specific level set algorithm [15]. Horsch et al. [16] presented a computationally efficient segmentation algorithm for breast masses on sonography, which is based on maximizing a utility function over partition margins defined through gray value thresholding of a preprocessed image. Their algorithm was evaluated on a database of 400 cases and the reported average overlap rate was 0.73. The challenge of applying contour-based method is to make sure the contour evolution is not trapped by non-breast edges. For region-based segmentation, both traditional methods and machine-learning-based pixel classification methods were investigated. Feng et al. [17] adopted an adaptive fuzzy C-means algorithm and the obtained DSC is 0.925. Pons et al. [18] reported that their evaluated automated method achieved a DSC of 0.49 using a Markov Random Field (MRF) and a Maximum a Posteriori (MAP) approach, by applying it to clinical data. Agarwal et al. [19] developed a semi-automatic framework for breast lesion segmentation in ABUS volumes which is based on the Watershed algorithm. Rodrigues et al. [20] took the advantage of pixel-wise classification and achieved a DSC of 0.824. Kumar et al. [21] proposed convolutional neural network approaches for breast ultrasound lesion segmentation and their algorithms effectively segmented the breast masses, achieving a mean DSC of 0.82.

As one branch of machine learning, deep learning has become popular as a self-taught approach in which features are computed in an automatic manner instead of combining manually designed features [22]–[27]. These approaches have rapidly become state-of-the-art that outperform other traditional methods in the segmentation tasks with ultrasound. There are generally two ways of applying deep learning: patch-wise classification using convolutional neural networks (CNN) and pixel-wise classification using fully convolutional networks (FCN) such as ResNet and U-Net architecture [28]. These techniques have gained propitiatory for the segmentation tasks. Most existing deep learning based methods still rely on image information (lesion boundaries) while the prior knowledge of breast lesion shape is not well used, although they have already obtained accurate segmentation results. To further improve classification results, proper incorporation of prior knowledge is necessary. In this work we use a model which tends to learn prior knowledge of breast lesions and is able to properly deal with fuzziness or even the absence of a visible lesion edge in some parts of lesions. We proposed a generative adversarial net (GAN) based framework, semi-pixel-wise cycle generative adversarial net (SPCGAN), for segmenting the lesion in 2D ultrasound images.

The main contributions of this work are as follows: 1. We propose a new breast lesion segmentation method that uses a deep learning approach where we combine the (cycle) GAN loss with a FCN loss (to also include a pixelwise classification). 2. We show clear improvements over existing lesion segmentation approaches on 2D ultrasound image datasets of breasts. The combination will make the segmentation not only reply on lesion boundary but also mimic the way of human annotation. Because of the power of GAN, the scheme requires less data to train a model with effectiveness and robustness.

II. METHODS

A. Semi-pixel-wise Cycle Generative Adversarial Net

Generative adversarial net (GAN) is a framework which consists of two models for the estimation of generative results via an adversarial process [29].

There is a generative model $G : \mathbb{R}^N \rightarrow C(\mathcal{N}, \mathbb{L}_1(\Omega))$ given by $\mathbf{w} \mapsto G_{\mathbf{w}}$ which tries to produce data that is similarly distributed as training data. Here the set of noisy images denoted by \mathcal{N} is obtained by sampling of uncorrelated Gaussian processes per position

$\mathbf{x} \in \Omega$ in the rectangular image domain $\Omega \subset \mathbb{R}^2$ on which all images are supported. Then given variable weights $\mathbf{w} \in \mathbb{R}^N$ it constructs a continuous mapping $G_{\mathbf{w}}$ from the set of noise images \mathcal{N} to a new set. Henceforth, this new set is called the set of fake images $\mathcal{F} := G_{\mathbf{w}}(\mathcal{N}) \subset \mathbb{L}_1(\Omega)$. We also have a set of true images $\mathcal{T} \subset \mathbb{L}_1(\Omega)$. In the training, we assign true images with label 1.

Simultaneously, a discriminative model $\mathbb{R}^M \ni \mathbf{v} \mapsto D_{\mathbf{v}}$ where operator $D_{\mathbf{v}} : \mathbb{L}_1(\Omega) \rightarrow \{0, 1\}$ evaluates the authenticity of a sample data coming from training set, and where \mathbf{v} are weights of the discriminative model. We apply a loss function to the pair of operators/models D and G to discriminate whether the input sample is real or not. Here both G and D aim to deteriorate the performance of each other, therefore the loss function of GANs mimics a two-player mini-max game and is expressed as follows:

$$\begin{aligned} & \min_{\mathbf{w} \in \mathbb{R}^N} \max_{\mathbf{v} \in \mathbb{R}^M} \mathcal{L}_{GAN}(D_{\mathbf{v}}, G_{\mathbf{w}}, \mathcal{T}, \mathcal{N}), \\ & \text{with the loss-function given by} \\ & \mathcal{L}_{GAN}(D_{\mathbf{v}}, G_{\mathbf{w}}, \mathcal{T}, \mathcal{N}) \\ & = \mathbb{E}_{p_{data}}[\log D_{\mathbf{v}}(\cdot)] + \mathbb{E}_p[\log(1 - D(G_{\mathbf{w}}(\cdot)))] \\ & = \frac{1}{|\mathcal{T}|} \sum_{f \in \mathcal{T}} \log(D_{\mathbf{v}}f) + \frac{1}{|\mathcal{N}|} \sum_{z \in \mathcal{N}} \log(1 - D_{\mathbf{v}}(G_{\mathbf{w}}z)). \end{aligned} \quad (1)$$

where \mathbf{w} are the weights for the generator model G and \mathbf{v} are the weights of the discriminator model D . The map $D_{\mathbf{v}}f$ gives the probability that data $f \in \mathbb{L}_1(\Omega)$ is a real image rather than a fake one (meaning there does not exist a noise image $f_0 \in \mathcal{N}$ such that $f = G_{\mathbf{w}}f_0$). Note that $p_{DATA}(f) = \frac{1}{|\mathcal{T}|}$ is a uniform distribution over the true images and p is a uniform distribution over the noisy images $p(z) = \frac{1}{|\mathcal{N}|}$ where $|\mathcal{N}|$ denotes the total number of noisy images (which is also the total number of fake images if $G_{\mathbf{w}}$ is injective).

Note that in (1) the distrimative model D is trained to maximize the probability to assign correct labels to input data $f \in \mathbb{L}_1(\Omega)$. Meanwhile, the generative model G is trained to disturb the judgment by the discriminative model D . Since the first term in (1) is independent of G this is done by minimizing the second term which is the expectation $\mathbb{E}_p[\log(1 - D_{\mathbf{v}}(G_{\mathbf{w}}(\cdot)))]$.

In a CycleGAN model [30], the generator no longer generates data from random source images \mathcal{N} such as white noise. There are two target domains $\mathcal{T}_1, \mathcal{T}_2 \subset \mathbb{L}_1(\Omega)$, which are sets of true images and which can be unpaired for data transfer between each other and the data generation process is now drawn in analogy to an autoencoder. There are two generators to translate data in one domain to the other, which can be regarded as an encoder and decoder respectively. There are also two discriminators and each of them tries to discriminate the authenticity of the data that belongs to the corresponding domain. Assume we have two real images $T_1, T_2 \in \mathbb{L}_1(\Omega)$ with $T_1 \in \mathcal{T}_1$ and $T_2 \in \mathcal{T}_2$, then the design of the CycleGAN model is as follows:

$$\{0, 1\} \xleftarrow{D_{\mathbf{v}_1}} T_1 \xrightleftharpoons[G_{\mathbf{w}_2}]{G_{\mathbf{w}_1}} F_2 \xrightarrow{D_{\mathbf{v}_2}} \{0, 1\}, \quad (2)$$

where $D_{v_k}(T_k) = 1$ if $T_k \in \mathcal{T}_k$ and 0 else, for $k = 1, 2$, and where fake images are given by $F_2 = G_{\mathbf{w}_1}T_1$ and $F_1 = G_{\mathbf{w}_2}T_2$.

Comparing to transfer data between target domains via two GANs, the cycle mechanism of CycleGAN network necessarily guarantees the one-to-one mapping relationship between the input and output data and therefore rules out the possibility that any input data can be mapped to induce a set of output data distributions which match the target domain [30].

Let us include a AB -labeling in G_{AB} to stress that it is a generative model from ‘domain’ A to ‘domain’ B which typically differs from the generative model G_{BA} from B to A . With domain

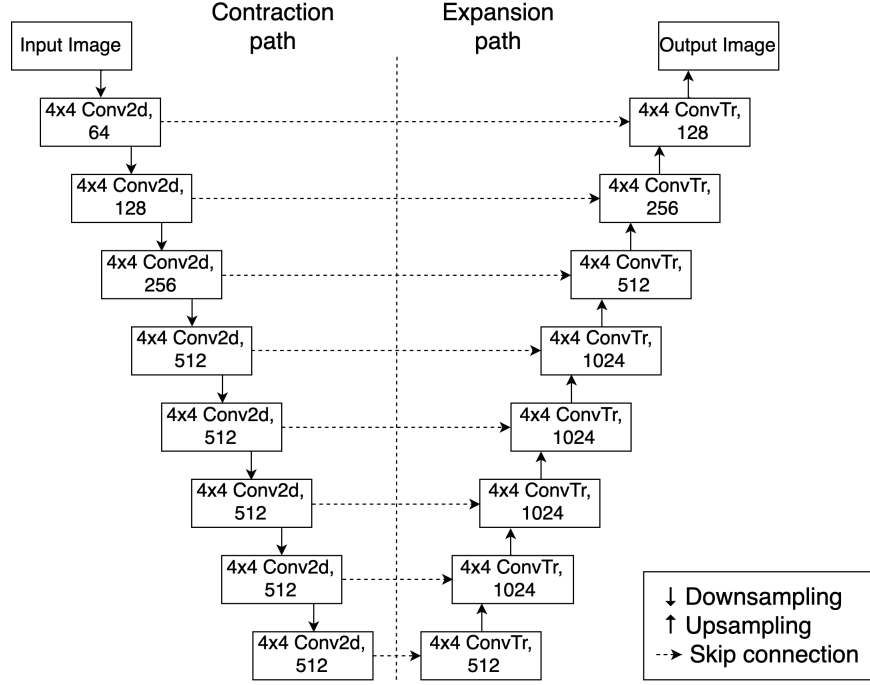


Fig. 2. The general architecture of the generators G_{AB} and G_{BA} in our model. It is an FCN based model and has the structure of U-Net. On the left side is the downsampling process which extracts the feature maps via convolutional layers from input image. On the right side is upsampling via convolutional transpose layers and connects with the feature map with upsampling result to get the final output.

we mean the joint set of the set of true images and fake images:

$$A = \mathcal{T}_1 \cup \mathcal{F}_1 \text{ and } B = \mathcal{T}_2 \cup \mathcal{F}_2, \text{ with } \mathcal{T}_i \cap \mathcal{F}_i = \emptyset, \quad (3)$$

where the sets $\mathcal{F}_1, \mathcal{F}_2$ of fake images are obtained by letting the generator act on the true-images of the other domain, i.e.

$$\mathcal{F}_1 = G_{BA, \mathbf{w}_2}(\mathcal{T}_2) \text{ and } \mathcal{F}_2 = G_{AB, \mathbf{w}_1}(\mathcal{T}_1). \quad (4)$$

Remark. In our application of segmenting lesions in ultrasound images, \mathcal{T}_1 is the set of ultrasound images without segmentation, and \mathcal{T}_2 is the set of manually segmented images. Then our generative convolutional network models are according to the design in Fig. 2 as we explain below. Then A and B are given by (3) and (4).

To ensure the expected mapping from input to the desired output, there is also a cycle loss to evaluate the decoder performance, which is to check whether the transformed data can be brought back to the original domain in the generative model transformation from domain B to domain A , and vice versa. This then provides cycle consistency in both forward and backward direction. Summarizing, we need

$$\begin{aligned} z &\rightarrow G_{BA, \mathbf{w}_2}(G_{AB, \mathbf{w}_1}(z)) \approx z \text{ for all } z \in \mathcal{T}_1, \\ z &\rightarrow G_{AB, \mathbf{w}_1}(G_{BA, \mathbf{w}_2}(z)) \approx z \text{ for all } z \in \mathcal{T}_2. \end{aligned}$$

To achieve this the cyclic loss function is expressed as follows:

$$\begin{aligned} \mathcal{L}_{cyc}(\mathbf{w}_1, \mathbf{w}_2, \mathcal{T}_1, \mathcal{T}_2) &= \\ &\mathbb{E}_{p_{dataA}} \left[\|G_{BA, \mathbf{w}_2}(G_{AB, \mathbf{w}_1})(\cdot) - (\cdot)\|_{L_1(\Omega)} \right] \\ &+ \mathbb{E}_{p_{dataB}} \left[\|G_{AB, \mathbf{w}_1}(G_{BA, \mathbf{w}_2})(\cdot) - (\cdot)\|_{L_1(\Omega)} \right] \\ &= \frac{1}{|\mathcal{T}_1|} \sum_{f \in \mathcal{T}_1} \int_{\Omega} |G_{BA, \mathbf{w}_2}(G_{AB, \mathbf{w}_1}(f))(\mathbf{x}) - f(\mathbf{x})| d\mathbf{x} \\ &+ \frac{1}{|\mathcal{T}_2|} \sum_{f \in \mathcal{T}_2} \int_{\Omega} |G_{AB, \mathbf{w}_1}(G_{BA, \mathbf{w}_2}(f))(\mathbf{x}) - f(\mathbf{x})| d\mathbf{x}. \end{aligned} \quad (5)$$

Eventually, in the CycleGAN model, the *total loss* \mathcal{L} is expressed as follows:

$$\begin{aligned} \mathcal{L}((\mathbf{w}_1, \mathbf{v}_1, \mathcal{T}_1), (\mathbf{w}_2, \mathbf{v}_2, \mathcal{T}_2)) &= \\ \mathcal{L}_{GAN}(D_{\mathbf{v}_1}, G_{\mathbf{w}_1}, \mathcal{T}_1, \mathcal{T}_2) &+ \mathcal{L}_{GAN}(D_{\mathbf{v}_2}, G_{\mathbf{w}_2}, \mathcal{T}_2, \mathcal{T}_1) \\ &+ \mathcal{L}_{cyc}(\mathbf{w}_1, \mathbf{w}_2, \mathcal{T}_1, \mathcal{T}_2) \end{aligned} \quad (6)$$

Now suppose optimization (1) is performed over the training dataset. This gives optimum $(\mathbf{w}_1^*, \mathbf{w}_2^*, \mathbf{v}_1^*, \mathbf{v}_2^*)$ that we hope to find efficiently by stochastic gradient descent in the usual deep learning approach.

Then given a test image $f \in \mathbb{L}_1(\Omega)$ the output segmentation is

$$\Omega \ni \mathbf{x} \mapsto (G_{AB, \mathbf{w}_1^*} f)(\mathbf{x}) \in \mathbb{R}, \quad (7)$$

where the output values are typically close to $\{0, 1\}$ due to the setting of manually segmented images in \mathcal{T}_2 in the training set.

In this work we adopt the general architecture of CycleGAN to our model and manipulate on the discriminator loss part by adding an extra loss related to the pixel-wise classification. This means that

$$\begin{aligned} \mathcal{L}^{NEW}((\mathbf{w}_1, \mathbf{v}_1, \mathcal{T}_1), (\mathbf{w}_2, \mathbf{v}_2, \mathcal{T}_2)) &= \\ = \mathcal{L}((\mathbf{w}_1, \mathbf{v}_1, \mathcal{T}_1), (\mathbf{w}_2, \mathbf{v}_2, \mathcal{T}_2)) &+ \mathcal{L}_{pix-wise}(\mathbf{w}_1, \mathcal{T}_1, \mathcal{T}_2). \end{aligned} \quad (8)$$

Now we have a correspondence between raw training images and their corresponding segmentation. Let us therefore write $f_1 \sim f_2$ if raw image $f_1 \in \mathcal{T}_1$ and manually segmented image $f_2 \in \mathcal{T}_2$ is indeed the segmentation of image f_1 . Note that $|\mathcal{T}_1| = |\mathcal{T}_2|$. Then we set

$$\mathcal{L}_{pix-wise}(\mathbf{w}_1, \mathcal{T}_1, \mathcal{T}_2) = \frac{1}{|\mathcal{T}_1|} \sum_{\substack{f_1 \in \mathcal{T}_1, \\ f_2 \in \mathcal{T}_2, \\ f_1 \sim f_2}} MSE(G_{BA, \mathbf{w}_1}(f_1), f_2), \quad (9)$$

where the Mean Square Error (MSE) is given by $MSE(f, g) = \frac{1}{|\Omega|} \int_{\Omega} |f(\mathbf{x}) - g(\mathbf{x})|^2 d\mathbf{x}$.

Our generator is a fully convolution neural network (FCN) shown in Figure 2 which only contains convolutional layers. FCN can be

trained end-to-end by upsampling and deconvoluting the feature maps extracted from convolutional layers and finally output pixel-wise classifications on the input images. It is widely used in semantic segmentations [31].

Now, we consider that \mathcal{T}_1 is the set of images without segmentation. \mathcal{T}_2 is the set of images with corresponding manual annotations. By adapting the loss function (9) the optimal weights ($\mathbf{v}_1^*, \mathbf{v}_2^*$) of the discriminative part are changed in such a way that discriminator stay close to the pixel-wise correct classifications for each pair (f_1, f_2) of ultrasound image $f_1 \in \mathcal{T}_1$ and its manual segmentation $f_2 \in \mathcal{T}_2$. This evaluates the adversarial loss between the manually annotated segmentation and the generated segmentation in every pixel (9):

Rather than just considering the probability of classifying the whole image in the forward process of the cycle, the discriminator tries to defy and reject the generated (pixel-wise) segmentation. Now the generator will minimize the pixel-wise loss so that the generated segmentations will be accepted by the discriminator. The architecture of our model is shown in Figure 3:

In the GAN-algorithm, the input data is drawn from a simple prior probability distribution such as a Gaussian distribution. Thereby, the input is essentially a latent vector of unstructured noise. The network learns to fold the probability distribution of the input data in the latent space to match as much as possible to the distribution of the target data. It is not able to take the advantage of the prior knowledge of images. However, in a CycleGAN-like algorithm, because there are two domains, we could draw the prior knowledge from the source image as the prior distribution and then generate samples based on it rather than imposing a random probability. In our implementation, the prior knowledge of annotated segmentation of breast lesions is learned by the model so that it is able to properly deal with images with ambiguous features, for example, in the absence of visible lesion edges.

B. Fully Convolutional Network (FCN)

The generator used above itself is an FCN and this type of network is applied extensively in ultrasound [32] [33] [34]–[37] [38] [39] for various applications.

To show the generic benefits of our model we tested with 2 different deep learning architectures (that is ResNet and U-Net) in the FCN part (given by Eq. 9) of our model.

To show the advantage of our model, we applied two networks for the FCN structure, U-Net and ResNet and compared the performances of our framework combined with these two structure models respectively. Throughout this manuscript we refer to U-net and ResNet as the "backbone" of the FCN. This is done to indicate the deep-learning architecture that underlies the FCN part of our model.

U-Net is a type of improved FCN. It can be regarded as two parts: the first half is in charge of the feature extraction as the convolutional layers work in CNN. The second half is to upsample the extracted feature which allows the context information to be propagated to higher resolution layers and output the segmented image as the same size as input. The U-Net structure we constructed in this experiment is shown in Fig. 2).

ResNet [40] aims to optimize the deteriorated performance of networks with very deep layers. It uses a residual block to create a shortcut connection in order to skip some of the convolutional layers. In this type of network, we could reduce the number of parameters so that the computation is simplified. The plain network architecture of ResNet keeps hierarchical configuration. The number of feature maps increase along with depth and the ability of feature extraction is therefore guaranteed. In our experiment, we applied a ResNet with 9 residual blocks as shown in Fig. 4 but modified to an FCN-like

model which contains downsampling and upsampling before and after residual calculation respectively. This modification makes our ResNet model adapt to the segmentation task rather than the classification as the original one does.

C. The Level Set Method

To compare our deep learning scheme with a traditional segmentation method, we applied a geodesic-active-contour (GAC) based level set method. This level set method includes curvature and advection terms as introduced by Caselles et al. [41]. The partial differential equation describing the motion of the contour is defined by:

$$\frac{\partial}{\partial t} \Phi + g \cdot (1 + \varepsilon k) |\nabla \Phi| + \alpha \nabla g \cdot \nabla \Phi = 0 \quad (10)$$

with $(\mathbf{x}, t) \rightarrow \Phi(\mathbf{x}, t)$ the level set function, ε the curvature influence, k the curvature of the level set, α the advection influence and g the image gradient-based speed function given by

$$g(\mathbf{x}) = 1 / (1 + |(\nabla G_s * f)(\mathbf{x})|), \quad (11)$$

where f is the input test image and $(\nabla G_s * f)(\mathbf{x})$ is the derivative of Gaussian operator applied at scale of $s = \frac{1}{2} \sigma^2$ with a standard-deviation that we manually set to $\sigma = \dots$ pixels. Note that the segmentation boundary is given by the 0-level set $\{\mathbf{x} \in \Omega \mid \Phi(\mathbf{x}, t) = 0\}$ where both the evolution time $t > 0$ and the parameters $\varepsilon, \alpha > 0$ are optimized via a gradient search algorithm applied on the training set, using the average Dice coefficient (12) criterium.

We initialize the level set with the center of the lesion. The segmentation can be controlled by setting the weights (α, ε) of propagation, curvature and advection term. The propagation term controls the inflation or 'balloon force' of the segmentation, the curvature term controls the 'smoothness' of the boundary of the segmentation and the advection term in the update equation attracts the contour to the lesion edge [14].

III. MATERIALS

A. Datasets

This study is based on 2D BUS DICOM images of abnormal patients. All DICOM images were scanned from SIEMENS MED SMS USG S2000 and TOSHIBA Aplio400 TUS-A400 Ultrasound System. For this study, we collected a dataset of 670 breast lesion ultrasound images from different women (aged 18-70) that had no history of breast cancer. Among the 670 images, 640 were scanned by a SIEMENS Ultrasound System and 30 were scanned by a TOSHIBA Ultrasound System. If there were a number of DICOM images from the same lesion, the DICOM image containing the maximum area of the lesion was collected into the dataset. The type of lesion has been clinically diagnosed as malignant or benign. Among the 640 lesions from SIEMENS Ultrasound System, 120 are malignant lesions and 520 are benign lesions.

In our study dataset, for SIEMENS images, 399 were used in the training phase, 141 were used in the testing phase and 100 were used in the validation phase. All TOSHIBA images were used for testing the generality of the model trained by SIEMENS images. During the image preprocessing stage, the original DICOM images were re-sampled to 0.1mm spacing in both horizontal and vertical directions. After that the ROI images were cropped from the re-sampled DICOM images with a size of 400*400 for easy processing, and the center of the lesions were the center of the ROI images.

For each ROI image, we manually generated reference lesion segmentations by using a MATLAB program. These manual segmentations were performed by an experienced researcher with 10 years of experience in breast ultrasound.

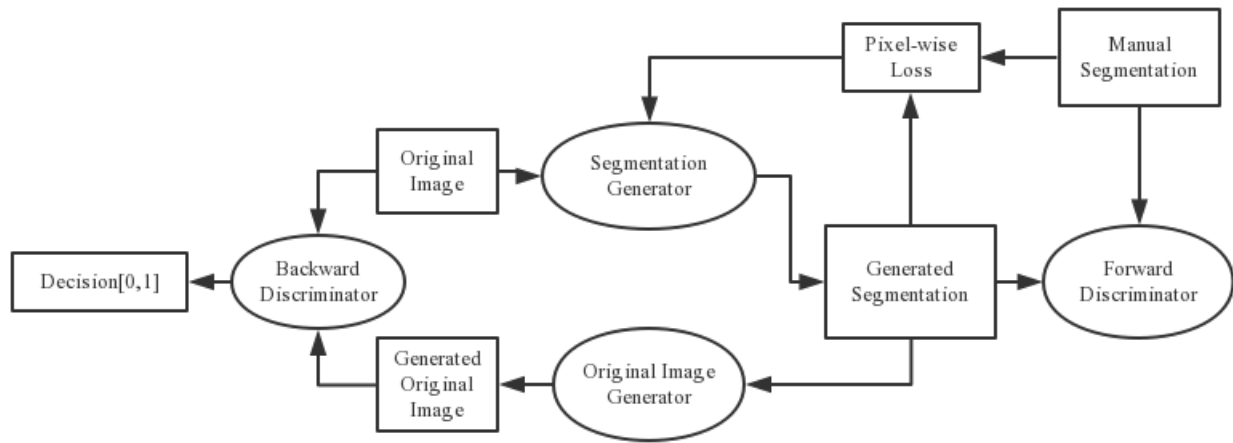


Fig. 3. The architecture of SPCGAN with pixel-wise loss. The pixel-wise loss is only applied in the forward cycle. In the forward cycle, the segmentation generator receives unsegmented original image and produces an auto-segmented image. The forward discriminator receives both auto-segmented and ground truth segmentation images to make pixel-wise classification. In the backward cycle, the auto-segmented image is fed into the backward generator to obtain a cyclic original image and input to the backward discriminator along with the real original one.

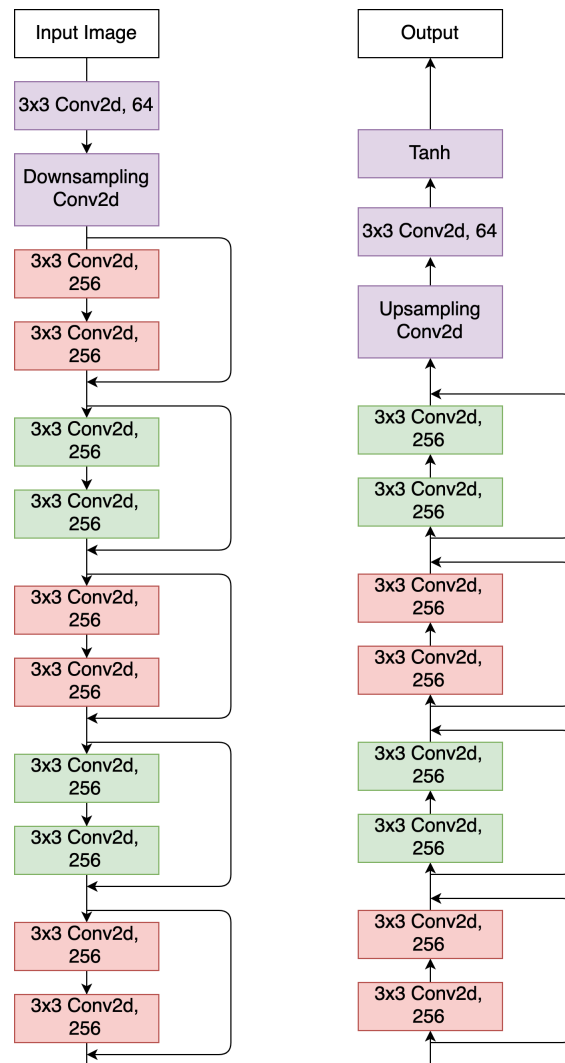


Fig. 4. The visualization of the structure of full convolutional networks, ResNet. The networks contains 9 residual blocks. Each block consists of two convolutional layers. Downsampling is performed on the input image before it was forward to the residual blocks and upsampled after it finished all the residual calculations. The size of input and output images are the same.

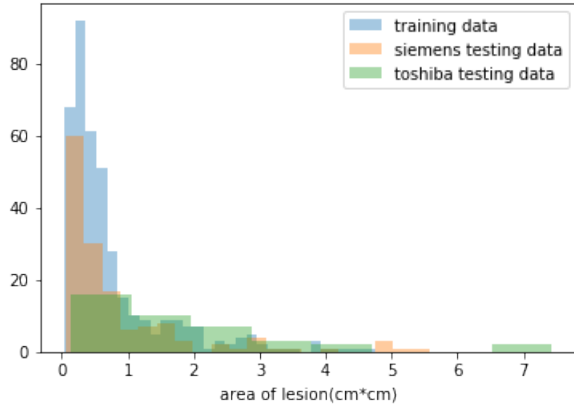


Fig. 5. The histogram of lesion areas in training and testing dataset.

B. Performance Evaluations

In this study, Dice similarity coefficient is used for describing the accuracy of the segmentation by different methods. Dice similarity coefficient is a statistic used for comparing the similarity between two samples, and is defined as follows:

$$DSC = \frac{2|X \cap Y|}{|X| + |Y|}, \quad (12)$$

where $|X|$ is the area of lesion by manual segmentation and $|Y|$ is the area of lesion segmented by automatic methods. The larger the Dice similarity coefficient is, the higher accuracy of the computational segmentation is. It ranges between 0 and 1.

C. Implementation platform

Our network was trained on a workstation equipped with an NVIDIA GeForce GTX 1080Ti GPU.

IV. EXPERIMENTS AND RESULTS

To show the superiority of our framework, we test SPCGAN, the backbone structure (ResNet) only and the level set method on both Siemens and Toshiba dataset. We also test the effectiveness of only applying generative adversarial networks framework with pixel-wise cost (GAN) without the cycle loss. To indicate the applicability of this framework, we also compare different frameworks but with a different backbone FCN structure (U-Net). For all experiments we performed training with the number of epochs 1500 with mini batch size 1, Adam optimizer [42] and without dropout. We use validation set to choose the model with least loss from different epochs.

We also apply the following data augmentation methods: shear (0.2 range), rotation (10 range), width shift (0.1 range), height shift (0.1 range), zoom (0.1 range), and horizontal flip to solve the problem of insufficient data.

A. Statistical Analysis

One-sided paired t-tests are used for statistical analysis when comparing results from different segmentation methods. The hypothesis in this study will be tested to control type I error rate at $\alpha = 0.05$. The hypothesis is that the DSC of the SPCGAN is superior to (bigger than) that of ResNet or the level set method, for statistical significance level $\alpha = 0.05$.

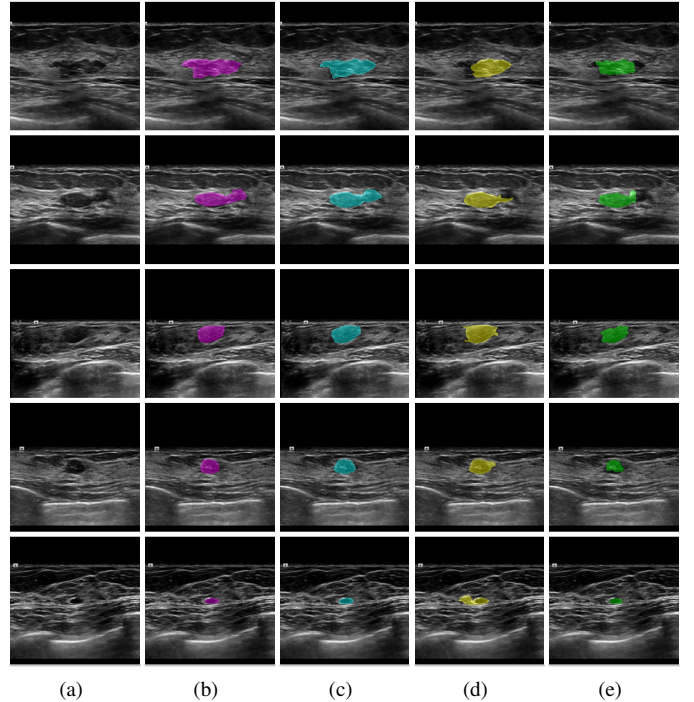


Fig. 6. Comparison of SPCGAN and other segmentation methods of benign lesions. (a) shows original image of benign lesions, (b) shows the manual annotation, (c) shows the result of SPCGAN, (d) and (e) show results from ResNet and level set.

TABLE I
DSC OF DIFFERENT SEGMENTATION METHODS.

	SPCGAN	FCN(ResNet)	level set
All lesions	0.92±0.04	0.90±0.07	0.79±0.17
benign	0.92±0.04	0.90±0.07	0.83±0.16
malignant	0.93±0.04	0.90±0.07	0.65±0.17

B. Comparisons among SPCGAN, FCN(ResNet) and Level Set

To evaluate the effect of SPCGAN framework on the breast ultrasound lesion segmentation accuracy, we compared it with FCN(ResNet) framework and the traditional segmentation method level set. Table I summarizes the DSC of different methods on our test database of 141 lesions from the entire dataset and 32 lesions are malignant. DSC values were obtained from 109 benign and 32 malignant breast lesions. Comparing the overall results of 3 different methods, we see that SPCGAN performed better by 2% improvement compared to the FCN(ResNet) method ($p < 0.001$). The traditional method level set performed significantly worse compared to SPCGAN method ($p < 0.001$). Furthermore, compared to the traditional segmentation method level set, the DSCs obtained from SPCGAN and FCN(ResNet) still remain high no matter a lesion is benign or malignant. The DSCs of malignant lesions from the level set method were much lower than the DSCs of benign lesions.

Fig.6 displays the segmentation results of our SPCGAN, FCN(ResNet) and the level set method from benign lesions. Compared with the FCN(ResNet) (d) and the level set (e) method, the results of our SPCGAN (c) show good agreements with the manual contours of the lesions. The segmentations from SPCGAN are very close to manual segmentations.

The examples given in Fig.7 correspond to the segmentation results of our SPCGAN, FCN(ResNet) and the level set method from malignant lesions. The FCN(ResNet) tends to oversegment the cancer

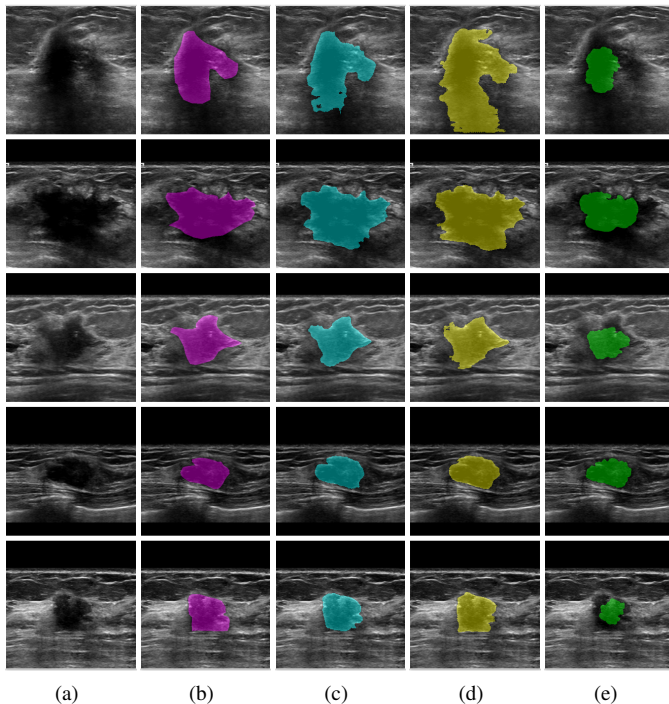


Fig. 7. Comparison of SPCGAN and other segmentation methods of malignant lesions.(a) shows original image of malignant lesions, (b) shows the manual annotation, (c) shows the result of SPCGAN ,(d) and (f) show results from FCN(ResNet) and the level set method.

when there is posterior shadowing, especially for the lesion in the first row. SPCGAN shows relatively more robust performance compared to FCN(ResNet) and the level set method.

Fig.8 illustrates boxplots of DSC for different segmentation methods. We can see that results from our SPCGAN have much less variance compared to other methods.

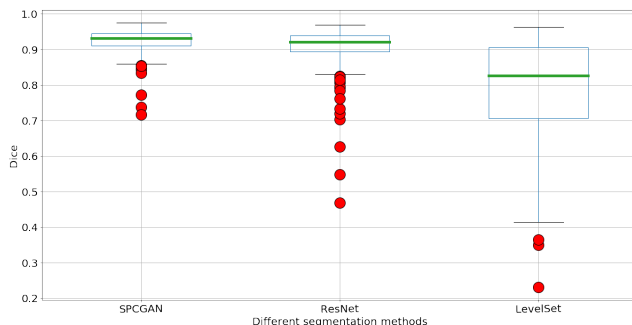


Fig. 8. Boxplot of DSC from different segmentation methods using backbone of ResNet.

C. Comparisons between Frameworks Trained with Varying Number of Samples

In order to compare the performance of SPCGAN, GAN and FCN(ResNet) model, we use varying numbers of samples to train the model and then test with the same testing dataset. The changes in the performance of SPCGAN, GAN and FCN(ResNet) when trained with 20, 40, 80, 200 and 399 samples are displayed in Fig. 9.

From Fig. 9 and Table II, we can observe that SPCGAN model obtained best results among all training sample numbers, especially when sample size was small. Although GAN and FCN(ResNet)

TABLE II
DSC OF DIFFERENT SEGMENTATION FRAMEWORKS USING BACKBONE OF RESNET.

number of training samples	SPCGAN	GAN	FCN
20	0.79 ± 0.26	0.74 ± 0.30	0.64 ± 0.37
40	0.85 ± 0.20	0.84 ± 0.22	0.83 ± 0.23
80	0.88 ± 0.10	0.86 ± 0.20	0.87 ± 0.15
200	0.91 ± 0.08	0.90 ± 0.08	0.90 ± 0.09
399	0.92 ± 0.04	0.91 ± 0.07	0.90 ± 0.07

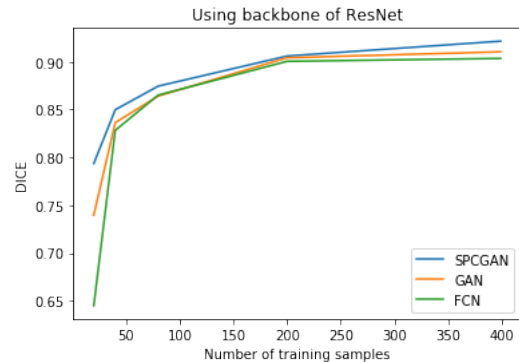


Fig. 9. DSC values obtained when SPCGAN ,GAN and FCN were trained with different number of training samples based on ResNet.

model trained with 200 samples can achieve DSC of 0.90, it is still 0.01 lower than SPCGAN. Particularly, when training samples increased to 399, the DSC of SPCGAN improved to 92% while that of FCN(ResNet) remained with 90%. The performance of GAN is between that of SPCGAN and FCN(ResNet).

Fig. 10 displays one case for which segmentation was performed by SPCGAN and FCN(ResNet) trained with varying numbers of samples. This example demonstrates how unclear boundary and shadow in ultrasound images may affect segmentation algorithms.

D. Results from Test Data from Other Manufactures

TABLE III
DSC FOR TOSHIBA IMAGES

	SPCGAN	GAN	FCN(ResNet)
30 test images	0.93 ± 0.02	0.92 ± 0.04	0.92 ± 0.04

To explore the performance of SPCGAN on the segmentation quality with test data from different manufactures, we collected 30 BUS images of breast disease scanned from TOSHIBA Ultrasound System and applied our model which was trained on SIEMENS images only.

From Table III, we can observe that the difference between DSC values of SPCGAN and FCN(ResNet) was not statistically significant ($p=0.14$ with paired t-test). The example given in Fig. 11 corresponds to a breast cancer with the ill-defined boundary. They are both very robust but the mean DSC from SPCGAN is still higher.

E. Comparisons among Models Trained with different backbone networks

In this section , we repeated the experiments where instead of using a ResNet method in the FCN part we use a U-Net method in the FCN part. From Fig. 12 and Table IV, we can observe that SPCGAN model still obtained best results among all training sample

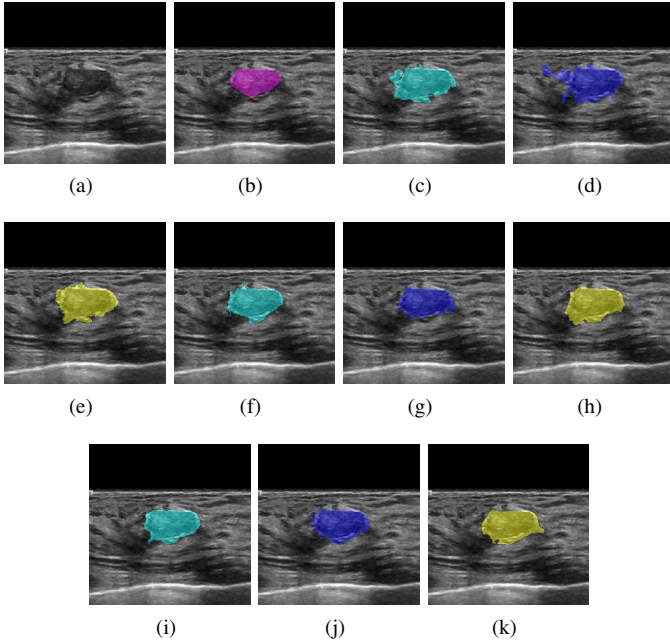


Fig. 10. A breast lesion, which was segmented by SPCGAN, GAN and FCN(ResNet) trained with varying number of samples. (a) shows the original image, (b) shows the manual annotation, (c) shows the result of SPCGAN with 20 training samples, (d) shows the result of GAN with 20 training samples, (e) shows the result of FCN(ResNet) with 20 training samples, (f) shows the result of SPCGAN with 200 training samples, (g) shows the result of GAN with 200 training samples, (h) shows the result of FCN(ResNet) with 200 training samples, (i),(j) and (k) show result of SPCGAN, GAN and FCN(ResNet) with 399 training samples respectively.

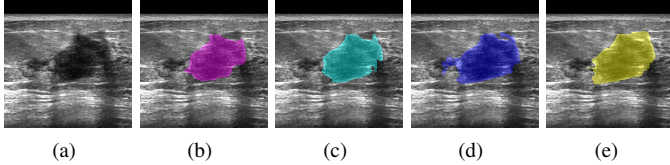


Fig. 11. Comparison among SPCGAN, GAN and FCN(ResNet) in a TOSHIBA image. (a) shows original image of benign lesions, (b) shows the manual annotation, (c) shows the result of SPCGAN, (d) shows the result of GAN, and (e) shows results from FCN(ResNet).

numbers. Table V and Table VI show the DSC of three different frameworks (SPCGAN, GAN and backbone structure only) based on two different backbone structures (ResNet and U-Net) on Siemens and Toshiba datasets. SPCGAN frame archives the best performance.

V. CONCLUSION AND DISCUSSION

In this study, we proposed a CycleGAN based model for segmenting breast lesions in 2D breast ultrasound. We compared our model with FCN and the level set based approach. The results show that our model is the most robust and accurate with a DSC of 0.92 ± 0.04 . Without retraining, the same model is applied on ultrasound images from a different manufacture, resulting a DSC of 0.93 ± 0.02 .

The novelty of our work is the combination of the CycleGAN and the pixel-wise cost which makes the model has the advantage of both GAN and FCN. The similar trends are observed for different frameworks with two different backbone structures (ResNet and U-Net). However, for some challenging images, especially when calcification is present, the segmentation is still not very smooth. From Figure 9, we can observe an improvement on DSC from 0.79

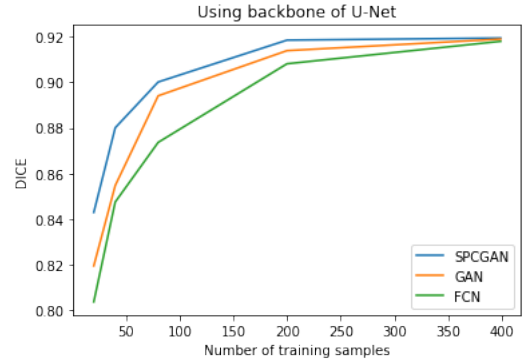


Fig. 12. DSC values obtained when SPCGAN, GAN and FCN were trained with different number of training samples based on U-Net.

TABLE IV

DSC OF DIFFERENT SEGMENTATION FRAMEWORKS USING BACKBONE OF U-NET.

number of training samples	SPCGAN	GAN	FCN
20	0.84±0.17	0.82±0.18	0.80±0.22
40	0.88±0.10	0.85±0.15	0.5±0.15
80	0.90±0.07	0.89±0.10	0.87±0.12
200	0.92±0.05	0.91±0.06	0.91±0.06
399	0.92±0.05	0.92±0.04	0.92±0.05

to 0.92 when the number of training images is increased. Another approach is to apply post processing, for example, Markov random filtering, to make segmentation smooth and complete. Both deep learning based methods are significantly better than the traditional level set approach in both malignant and benign cases, even when the deep learning model is only trained with 20% percent of the dataset. With more annotated data, the performance of supervised learning can be improved significantly. It is still possible to enhance the segmentation performance by combining deep learning methods with geometric methods that take into account the context of local orientations (in the images and/or segmentation boundaries) via group-CNNs [43] instead of the normal CNNs (FCNs) used in this paper.

In the cyclic training process of our model, the forward generator firstly produces automatic segmentation of the breast lesions indistinguishable to the forward discriminator by minimizing the adversarial loss, cycle consistency loss and pixel-wise cost. This generated segmentation is then fed into the backward generator which tries to get it recover to the original image. During this stage, the

TABLE V

DSC FOR SIEMENS IMAGES TESTED BY DIFFERENT SEGMENTATION MODELS TRAINED WITH DIFFERENT BACKBONE NETWORKS.

	SPCGAN	GAN	backbone only
ResNet	0.92±0.04	0.91±0.06	0.90±0.07
U-Net	0.92±0.04	0.92±0.04	0.92±0.05

TABLE VI

DSC FOR TOSHIBA IMAGES TESTED BY DIFFERENT SEGMENTATION MODELS TRAINED WITH DIFFERENT BACKBONE NETWORKS.

	SPCGAN	GAN	backbone only
ResNet	0.93±0.02	0.92±0.04	0.92±0.04
U-Net	0.94±0.02	0.94±0.02	0.93±0.02

pixel-wise cost is no longer applied as it is hard to recover the original image from the segmentation at a pixel level. The implementation of CycleGAN algorithm effectively utilizes the prior knowledge of lesion images to provide the prior distribution in the latent space for the input. By imposing this prior probability distribution, the mapping between input data sample and real data is under a more sensible constraint. In ultrasound annotation tasks, the segmentation is challenging because of poor quality, posterior shadowing and weak boundaries. In this case, the use of prior knowledge could further improve the robustness of the segmentation.

Accurate segmentation would help describe shape, orientation, margins, echo pattern, posterior acoustic features, and surrounding tissue alterations of a lesion in BI-RADS US lexicon. The description would also aid radiologists or computer algorithms [9], [10] to diagnose a lesion. Given accurate segmentations, it would be logical to design further deep learning networks to differentiate malignant lesions from benign lesions or generate BI-RADS scores in ultrasound.

One limitation of our study is that we compared the segmentation results to annotations from only one medical expert. Although beyond the scope of the present work, it is of interest to include multiple annotations by several medical experts. Moreover, as the CycleGAN model has the ability of learning prior knowledge, for example the shape, it is possible that it only learns the style of one reader. Whether the prior knowledge from one reader is sufficient to obtain good inter-reader variability shall be investigated in the future.

In the real clinical practice, there are ultrasound devices from different manufacturers deployed. These images vary in resolution, contrast, and the presence of noise. In this study, we evaluated the possibility of applying our deep learning model trained on SIEMENS ultrasound images only to TOSHIBA ultrasound images. The segmentation accuracy still remains high. Researchers can focus on developing robust algorithms on different types of ultrasound images, which is important to make computer techniques available to real world practice.

In this work we focused on segmenting a specific type of lesions in ultrasound images of breasts. As a result we take advantage both of the GAN (acting globally on full images) and of the FCN (with a pixel-wise loss to account for local optimization) in our unifying machine learning approach for lesion segmentation. Our method has the potential to help radiologists delineate breast lesion and improve the efficiency of workflow for reporting and inter-/intra- reader variability. As we achieved promising results on our two datasets, it is also interesting to apply the technique to other segmentation problems in medical imaging. While focused on one type of lesions in ultrasound, future work can address a wider range of objects in different medical images.

REFERENCES

- [1] C DeSantis, R Siegel, and A Jemal. Breast cancer facts & figures 2015-2016. atlanta: American cancer society. Inc, 2015:1–44, 2015.
- [2] Kamlesh Kaul and Fabienne Marie-Louise Daguilh. Early detection of breast cancer: is mammography enough? *Hospital Physician*, 38(9):49–54, 2002.
- [3] H. Laine, J. Rainio, H. Arko, and T. Tukeyva. Comparison of breast structure and findings by X-ray mammography, ultrasound, cytology and histology: A retrospective study. *European Journal of Ultrasound*, 2(2):107–115, April 1995.
- [4] Vittorio Corsetti, Nehmat Houssami, Aurora Ferrari, Marco Ghirardi, Sergio Bellarosa, Osvaldo Angelini, Claudio Bani, Pasquale Sardo, Giuseppe Remida, Enzo Galligioni, et al. Breast screening with ultrasound in women with mammography-negative dense breasts: evidence on incremental cancer detection and false positives, and associated cost. *European journal of cancer*, 44(4):539–544, 2008.
- [5] Qing-Kun Song, Xiao-Li Wang, Xin-Na Zhou, Hua-Bing Yang, Yu-Chen Li, Jiang-Ping Wu, Jun Ren, and Herbert Kim Lyerly. Breast cancer challenges and screening in china: lessons from current registry data and population screening studies. *The oncologist*, 20(7):773–779, 2015.
- [6] Carl J D’Orsi. *ACR BI-RADS atlas: breast imaging reporting and data system*. American College of Radiology, 2013.
- [7] Ehsan Kozegar, Mohsen Soryani, Hamid Behnam, Masoumeh Salamati, and Tao Tan. Breast cancer detection in automated 3d breast ultrasound using iso-contours and cascaded rusboosts. *Ultrasonics*, 79:68–80, 2017.
- [8] Tao Tan, Jan-Jurre Mordang, Jan Zelst, André Grivegnée, Albert Gubern-Mérida, Jaime Melendez, Ritse M Mann, Wei Zhang, Bram Platel, and Nico Karssemeijer. Computer-aided detection of breast cancers using haar-like features in automated 3d breast ultrasound. *Medical physics*, 42(4):1498–1504, 2015.
- [9] Tao Tan, Bram Platel, Roel Mus, Laszlo Tabar, Ritse M Mann, and Nico Karssemeijer. Computer-aided detection of cancer in automated 3-d breast ultrasound. *IEEE transactions on medical imaging*, 32(9):1698–1706, 2013.
- [10] Tao Tan, Bram Platel, Henkjan Huisman, Clara I Sánchez, Roel Mus, and Nico Karssemeijer. Computer-aided lesion diagnosis in automated 3-d breast ultrasound using coronal spiculation. *IEEE transactions on medical imaging*, 31(5):1034–1042, 2012.
- [11] Tao Tan, Bram Platel, Thorsten Twellmann, Guido van Schie, Roel Mus, André Grivegnée, Ritse M Mann, and Nico Karssemeijer. Evaluation of the effect of computer-aided classification of benign and malignant lesions on reader performance in automated three-dimensional breast ultrasound. *Academic radiology*, 20(11):1381–1388, 2013.
- [12] Haixia Liu, Tao Tan, Jan van Zelst, Ritse Mann, Nico Karssemeijer, and Bram Platel. Incorporating texture features in a computer-aided breast lesion diagnosis system for automated three-dimensional breast ultrasound. *Journal of Medical Imaging*, 1(2):024501, 2014.
- [13] Jing Cui, Berkman Sahiner, Heang-Ping Chan, Alexis Nees, Chintana Paramagul, Lubomir M Hadjiiski, Chuan Zhou, and Jiazheng Shi. A new automated method for the segmentation and characterization of breast masses on ultrasound images. *Medical physics*, 36:1553–1565, May 2009.
- [14] Tao Tan, Albert Gubern-Mérida, Cristina Borelli, Rashindra Maniensing, Jan van Zelst, Lei Wang, Wei Zhang, Bram Platel, Ritse M Mann, and Nico Karssemeijer. Segmentation of malignant lesions in 3d breast ultrasound using a depth-dependent model. *Medical physics*, 43:4074, July 2016.
- [15] E Kozegar, M Soryani, H Behnam, M Salamati, and T Tan. Mass segmentation in automated 3-d breast ultrasound using adaptive region growing and supervised edge-based deformable model. *IEEE transactions on medical imaging*, 37:918–928, April 2018.
- [16] K Horsch, M L Giger, L A Venta, and C J Vyborny. Automatic segmentation of breast lesions on ultrasound. *Medical physics*, 28:1652–1659, August 2001.
- [17] Yuan Feng, Fenglin Dong, Xiaolong Xia, Chun Hong Hu, Qianmin Fan, Y Hu, Mingyuan Gao, and S Mutic. An adaptive fuzzy c-means method utilizing neighboring information for breast tumor segmentation in ultrasound images. *Medical Physics*, 44(7):3752–3760, 2017.
- [18] Gerard Pons, Joan Martí, Robert Martí, Sergi Ganau, and J Alison Noble. Breast-lesion segmentation combining b-mode and elastography ultrasound. *Ultrasonic imaging*, 38:209–224, May 2016.
- [19] Richa Agarwal, Oliver Diaz, Xavier Llad, Albert Gubern-Mérida, Joan C Vilanova, and Robert Martí. Lesion segmentation in automated 3d breast ultrasound: Volumetric analysis. *Ultrasonic imaging*, 40:97–112, March 2018.
- [20] Rafael Rodrigues, Rui Braz, Manuela Pereira, Jos Moutinho, and Antonio M G Pinheiro. A two-step segmentation method for breast ultrasound masses based on multi-resolution analysis. *Ultrasound in medicine & biology*, 41:1737–1748, June 2015.
- [21] Viksit Kumar, Jeremy M Webb, Adriana Gregory, Max Denis, Duane D Meixner, Mahdi Bayat, Dana H Whaley, Mostafa Fatemi, and Azra Alizad. Automated and real-time segmentation of suspicious breast masses using convolutional neural network. *PLoS one*, 13:e0195816, 2018.
- [22] Alex Krizhevsky, Ilya Sutskever, and Geoffrey E. Hinton. Imagenet classification with deep convolutional neural networks. *Commun. ACM*, 60(6):84–90, May 2017.
- [23] Kaiming He, Xiangyu Zhang, Shaoqing Ren, and Jian Sun. Identity mappings in deep residual networks. In *European Conference on Computer Vision*, pages 630–645, 2016.
- [24] Sergey Ioffe and Christian Szegedy. Batch normalization: Accelerating deep network training by reducing internal covariate shift. In *International Conference on Machine Learning*, pages 448–456, 2015.

- [25] Gao Huang, Zhuang Liu, Kilian Q Weinberger, and Laurens van der Maaten. Densely connected convolutional networks. *arXiv preprint arXiv:1608.06993*, 2016.
- [26] T. Tan, Z. Li, H. Liu, F. G. Zanjani, Q. Ouyang, Y. Tang, Z. Hu, and Q. Li. Optimize transfer learning for lung diseases in bronchoscopy using a new concept: Sequential fine-tuning. *IEEE Journal of Translational Engineering in Health and Medicine*, 6:1–8, 2018.
- [27] Dongsheng Jiang, Weiqiang Dou, Luc Vosters, Xiayu Xu, Yue Sun, and Tao Tan. Denoising of 3d magnetic resonance images with multi-channel residual learning of convolutional neural network. *Japanese journal of radiology*, 36(9):566–574, 2018.
- [28] Olaf Ronneberger, Philipp Fischer, and Thomas Brox. U-net: Convolutional networks for biomedical image segmentation. In *International Conference on Medical image computing and computer-assisted intervention*, pages 234–241. Springer, 2015.
- [29] Ian Goodfellow, Jean Pouget-Abadie, Mehdi Mirza, Bing Xu, David Warde-Farley, Sherjil Ozair, Aaron Courville, and Yoshua Bengio. Generative adversarial nets. In *Advances in neural information processing systems*, pages 2672–2680, 2014.
- [30] Jun-Yan Zhu, Taesung Park, Phillip Isola, and Alexei A Efros. Unpaired image-to-image translation using cycle-consistent adversarial networks. In *Computer Vision (ICCV), 2017 IEEE International Conference on*, 2017.
- [31] Jonathan Long, Evan Shelhamer, and Trevor Darrell. Fully convolutional networks for semantic segmentation. In *Proceedings of the IEEE conference on computer vision and pattern recognition*, pages 3431–3440, 2015.
- [32] Yizhe Zhang, Michael TC Ying, Lin Yang, Anil T Ahuja, and Danny Z Chen. Coarse-to-fine stacked fully convolutional nets for lymph node segmentation in ultrasound images. In *Bioinformatics and Biomedicine (BIBM), 2016 IEEE International Conference on*, pages 443–448. IEEE, 2016.
- [33] Moi Hoon Yap, Gerard Pons, Joan Martí, Sergi Ganau, Melcior Sentís, Reyer Zwiggelaar, Adrian K Davison, and Robert Martí. Automated breast ultrasound lesions detection using convolutional neural networks. *IEEE journal of biomedical and health informatics*, 2017.
- [34] Hariharan Ravishankar, S Thiruvankadam, R Venkataramani, and V Vaidya. Joint deep learning of foreground, background and shape for robust contextual segmentation. In *International Conference on Information Processing in Medical Imaging*, pages 622–632. Springer, 2017.
- [35] Lingyun Wu, Yang Xin, Shengli Li, Tianfu Wang, Pheng-Ann Heng, and Dong Ni. Cascaded fully convolutional networks for automatic prenatal ultrasound image segmentation. In *Biomedical Imaging (ISBI 2017), 2017 IEEE 14th International Symposium on*, pages 663–666. IEEE, 2017.
- [36] Ozan Oktay, Enzo Ferrante, Konstantinos Kamnitsas, Mattias Heinrich, Wenjia Bai, Jose Caballero, Stuart A Cook, Antonio de Marvao, Timothy Dawes, Declan P O’Regan, et al. Anatomically constrained neural networks (acnns): application to cardiac image enhancement and segmentation. *IEEE transactions on medical imaging*, 37(2):384–395, 2018.
- [37] Fausto Milletari, Seyed-Ahmad Ahmadi, Christine Kroll, Annika Plate, Verena Rozanski, Juliana Maiostre, Johannes Levin, Olaf Dietrich, Birgit Ertl-Wagner, Kai B?tzl, and Nassir Navab. Hough-CNN: Deep learning for segmentation of deep brain regions in MRI and ultrasound. *Computer Vision and Image Understanding*, 164:92–102, November 2017.
- [38] V. Sundaresan, C. P. Bridge, C. Ioannou, and J. A. Noble. Automated characterization of the fetal heart in ultrasound images using fully convolutional neural networks. In *Proc. IEEE 14th Int. Symp. Biomedical Imaging (ISBI 2017)*, pages 671–674, April 2017.
- [39] L. Wu, Y. Xin, S. Li, T. Wang, P. A. Heng, and D. Ni. Cascaded fully convolutional networks for automatic prenatal ultrasound image segmentation. In *Proc. IEEE 14th Int. Symp. Biomedical Imaging (ISBI 2017)*, pages 663–666, April 2017.
- [40] Kaiming He, Xiangyu Zhang, Shaoqing Ren, and Jian Sun. Deep residual learning for image recognition. *CoRR*, abs/1512.03385, 2015.
- [41] Vicent Caselles, Ron Kimmel, and Guillermo Sapiro. Geodesic active contours. *International Journal of Computer Vision*, 22(1):61, February 1997.
- [42] Diederik P Kingma and Jimmy Ba. Adam: A method for stochastic optimization. *international conference on learning representations*, 2015.
- [43] E J Erik Bekkers, Maxime W Lafarge, Mitko Veta, Koen A J Eppenhof, Josien P W Pluim, and R Remco Duits. Roto-translation covariant convolutional networks for medical image analysis. *medical image computing and computer assisted intervention*, pages 440–448, 2018.